A Simple and Sensitive Approach for Real-Time Sensing of Enzymatically Catalyzed Hydrogelation

Sebastian Putz, Meriem Kassar, Claude Oelschlaeger, Matthias Franzreb,* and Gözde Kabay*

Despite the critical role of hydrogels in material science and biotechnology, current methods for analyzing their formation lack real-time monitoring and require complex sample preparation and instrumentation. In this work, an innovative methodology is introduced for the real-time analysis of enzymatically catalyzed hydrogelation. Electrochemical impedance spectroscopy (EIS) coupled with interdigitated electrodes (IDEs) to sense and transduce the gelation reaction of model precursor carboxymethyl cellulose-tyramine (CMC-TA) conjugates that undergoes enzymatic cross-linking by horseradish peroxidase (HRP) and hydrogen peroxide (H_2O_2). Real-time monitoring involves single-frequency analyses at 3×10^5 Hz, where the measured impedance consists solely of a resistive component, and the admittance equates to solution conductance. The gelation trajectories for all tested enzymatically cross-linked hydrogel component combinations are determined by substituting the conductance data in the modified Michaelis–Menten kinetic model. Specifically, for CMC-TA cross-linked by HRP, the authors calculate apparent K_M and k_{cat} values of 82.1 µM and 95.5 s^{-1}, respectively. These findings are further validated through rheological characterization, including oscillatory shear measurements and microrheology. Overall, this research paves the way for a streamlined, accurate, and cost-effective approach to controllable enzymatically initiated hydrogel synthesis, enhancing their successful application in various fields ranging from material science to biotechnology.

1. Introduction

Hydrogels are 3D cross-linked polymer networks capable of absorbing and retaining large amounts of water.[1] They possess exceptional biocompatibility, elasticity, and the potential for functionalization to achieve desired properties for a specific application. These unique features make them indispensable in various biomedical applications, including tissue engineering,[2,3] wound healing,[4–6] bioprinting,[7] drug delivery,[8] and sensing[9,10] applications.

Enzymatically cross-linked hydrogels received particular interest because using enzymes for cross-linking offers several inherent advantages. Enzymes provide substrate and reaction specificity, minimizing the formation of unwanted and potentially toxic side products, crucial in biomedical applications. Additionally, enzymatic reactions occur under mild conditions, aligning with the needs of biological organisms. Numerous attempts have been made to produce rapidly forming hydrogels using enzymes such as transglutaminases, tyrosinases, lysyl oxidases, phosphatases, and peroxidases.[11]

Horseradish peroxidase (HRP) stands out among the enzymes used for cross-linking, offering highly controllable cross-linking ability for tailoring hydrogels' properties and gelation kinetics.[12,13] Consequently, multiple research groups have produced and characterized HRP-cross-linked hydrogels, including polymer-phenol-conjugates of carboxymethyl cellulose,[12] gelatin,[13,14] hyaluronic acid,[15,16] polyethylene glycol[17] and alginate,[18,19] and many show great promise in particularly wound healing,[20] tissue engineering,[21,22] and drug delivery[16] applications.

Briefly, HRP catalyzes the decomposition of hydrogen peroxide (H_2O_2) or other peroxides by utilizing aromatic proton donors as substrates. In this redox reaction, H_2O_2 is reduced to H_2O, while the aromatic proton donor is oxidized to form a radical product.[23] During a single catalytic cycle, two radicals are generated, consuming one molecule of H_2O_2. Various functional groups, including aromatic phenols, amines, and phenolic acids, can serve as reducing substrates. However, phenols are the most employed due to their high specificity,

S. Putz, M. Kassar, M. Franzreb, G. Kabay
Karlsruhe Institute of Technology (KIT)
Institute of Functional Interfaces (IFG)
Department for Bioengineering and Biosystems
76344 Eggenstein-Leopoldshafen, Germany
E-mail: gozde.kabay@kit.edu; matthias.franzreb@kit.edu
C. Oelschlaeger
Karlsruhe Institute of Technology (KIT)
Institute of Mechanical Process Engineering and Mechanics (MVM)
Department for Applied Mechanics (AME)
76131 Karlsruhe, Germany

ADVANCED
SCIENCE NEWS

www.advancedsciencenews.com

ADVANCED
FUNCTIONAL
MATERIALS

www.afm-journal.de

efficiency, biocompatibility, availability, tunable reactivity, stability, controlled cross-linking, versatility, and low toxicity.[23] When phenol groups are linked to polymer chains, the subsequent reaction of two radicals initiates the cross-linking of adjacent polymer chains, forming a hydrogel precursor. A 3D hydrogel network is created through extensive cross-linking.[21] Figure S1 (Supporting Information) illustrates the enzymatic cross-linking reaction of a polymeric hydrogel precursor containing phenol and carboxyl groups, representing the scenario examined in this study: the tyramine-conjugated carboxymethyl cellulose (CMC-TA) precursor catalyzed by the HRP enzyme in the presence of H_2O_2. The depiction is simplified, as the catalytic cycle encompasses multiple steps involving intermediate compounds.[23]

It is important to emphasize that understanding and optimizing gelation kinetics is crucial for tailoring hydrogel properties for intended applications.[24] Current methods utilized for investigating hydrogelation processes, such as oscillatory shear rheology,[25] multiple particle tracking,[26] Cryo-TEM,[27] and X-ray scattering,[28] are resource-intensive, laborious, and require extensive sample preparation. These challenges often limit the accessibility of hydrogel research to a broader scientific community and hinder its rapid progress.

In response to these limitations, we propose a novel approach centered on electrochemical impedance spectroscopy (EIS) analysis. EIS is an electroanalytical technique used to measure the impedance of an electrochemical cell across a range of frequencies when an alternating current (AC) voltage is applied. The data reveal crucial characteristics of the electrode-electrolyte interface and the bulk electrolyte. Analyzing the system across a wide range of frequencies enables distinguishing between processes occurring at different time scales. Unlike conventional techniques, it requires minimal sample preparation and operates with a simple experimental setup. By employing EIS in conjunction with interdigitated electrodes (IDEs), fast and sensitive detection[32] of the tested samples, even at lower volumes,[29] can be ensured. Consequently, we hypothesized that EIS is a promising approach for the rapid, sensitive, and real-time investigation of hydrogelation reactions. After screening a series of CMC-TA hydrogelation reactions catalyzed by the HRP enzyme in the presence of H_2O_2, our hypothesis was confirmed, as it allowed accurate prediction of each gelation reaction´s time course data, which was later fitted to the modified Michaelis-Menten kinetic model for real-time assessment of enzymatically mediated hydrogelation and extracting corresponding kinetic parameters.

Furthermore, EIS is a well-established technique in various fields, including investigations related to batteries,[30] corrosion processes,[31] and semiconductor characterization.[32] Building on this foundation, our pioneering application of EIS to study hydrogelation reaction kinetics represents a groundbreaking extension of this electrochemical technique into material research. This approach simplifies hydrogel analysis and opens new possibilities for precise control and optimization of hydrogel properties, holds the promise of advancing their utility in diverse biomedical applications.

2. Results and Discussion

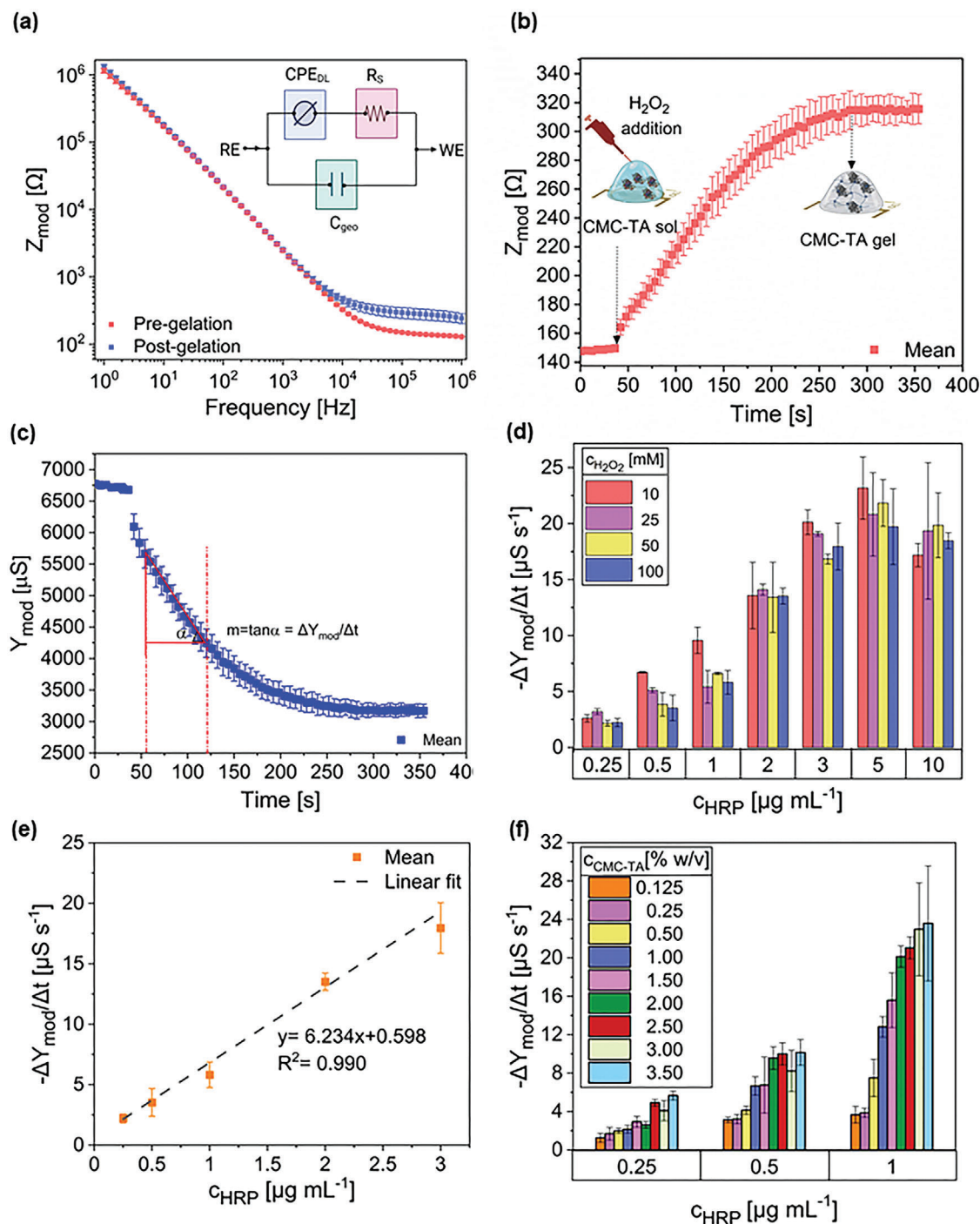### 2.1. Characterization of Carboxymethyl Cellulose-Tyramine Conjugates (CMC-TA)

UV–vis and ^{1}H-NMR spectroscopy analyses were conducted to characterize the synthesized CMC-TA precursors. The UV–vis spectrum of the synthesized CMC-TA showed that 0.561 µmol mg^{-1} of phenol was incorporated into the CMC. The successful synthesis of the CMC-TA precursor was also confirmed by ^{1}H-NMR spectral readings, which showed newly formed peaks at ≈6.8 and 7.0 ppm in comparison to the unconjugated CMC, indicating the aromatic protons of the conjugated tyramine.[33] The UV–vis spectra and images of the lyophilized CMC-TA, CMC-TA dissolved in UPW, and the CMC-TA hydrogel can be found in the Supporting Information (Figure S2). Additionally, ^{1}H-NMR spectra of all gel-forming components are given in Figure S3, Supporting Information.

2.2. Establishing an Impedimetric Sensing Method for Gelation Reaction Monitoring

First, potentiostatic EIS scans were performed to screen the electrical properties of CMC-TA before and after gelation (**Figure 1A**). The impedance spectra are represented as Bode plots, where the impedance modulus (Z_{mod}) is plotted against the frequency on the logarithmic scale. The results showed that Z_{mod} significantly increased, particularly between 1×10^5 and 1×10^6 Hz, after the gelation reaction of CMC-TA precursor was initiated.

Following EIS analysis, we subjected the acquired impedance spectra to fitting using the equivalent circuit model (Figure 1a inset) to comprehend the alterations in electrical properties resulting from the gelation reaction. Numerical values for the circuit elements, double-layer capacitance (CPE_{DL}), geometric capacitance (C_{geo}), and the solution resistance (R_s) are extracted (Table S1, Supporting Information). Fitting the data to the equivalent circuit model revealed that the C_{geo} increased by about 15%, which can be attributed to a higher relative permittivity of the formed gel compared to the precursor mixture. In contrast, the CPE_{DL} exhibited a slight decrease of about 10% after gelation. As the CPE_{DL} value depends on the ion concentration in the solution, the reduced ion concentration that resulted from diluting the CMC-TA and HRP mixture with H_2O_2 addition, which was supplied to initiate the gelation, resulted in decreasing CPE_{DL}.[34] However, the most significant gelation effect was observed in the solution resistance, R_s, which more than doubled after gelation (from 136.5 ± 1.5 to 284.7 ± 44.2 Ω). The increase in R_s is hypothesized to originate from the reduced ion mobility caused by the formation of the porous gel network and the increased viscosity of the surrounding solution. As previously described, the reduced mobility of charged species is mainly due to the increased size of cross-linked precursor molecules. Thus, as the charged precursor molecules and the corresponding counter-ions are the system's dominant conductivity source, the measured solution resistance rises considerably.

Due to the substantial increase during gelation, the impedance in the frequency region between 1×10^5 and 1×10^6 Hz was

**ADVANCED
SCIENCE NEWS**

www.advancedsciencenews.com

**ADVANCED
FUNCTIONAL
MATERIALS**

www.afm-journal.de

Figure 1. a) Bode spectra of 2.00% w/v CMC-TA precursor before and after initiating gelation reaction with 3.00 µg mL^{-1} HRP and 50 mM H$_2$O$_2$. The equivalent circuit is sketched as the figure inset used for data fitting. b) Exemplary single frequency impedance measurements of 2.00% w/v CMC-TA precursor gelated with 50 mM H$_2$O$_2$ and 3.00 µg mL^{-1} HRP. c) The exact single frequency measurement data converted from impedance (Z_{mod}) to admittance (Y_{mod}) modulus. d) The effect of HRP and H$_2$O$_2$ concentrations on the gelation rate is represented by the slope of Y_{mod} obtained from single frequency measurements conducted for 2.00% w/v CMC-TA. e) The plot describes the linear relationships between HRP concentration and the slope of Y_{mod}. f) The effect of CMC-TA concentration on the slope of Y_{mod}. The data points represent the mean values, and the error bars indicate the standard deviation of replicated experiments ($n = 3$).

ADVANCED
SCIENCE NEWS
www.advancedsciencenews.com

ADVANCED
FUNCTIONAL
MATERIALS
www.afm-journal.de

chosen as the best metric to evaluate the reaction kinetics. Therefore, in the second step of the analysis, single frequency measurements at 3×10^5 Hz were performed to monitor the hydrogelation process in a time-resolved manner. The experimental procedure established for evaluating the gelation reaction is sketched in the Supporting Information (Figure S4).

The results of exemplary single frequency measurements for 2.00% w/v CMC-TA using a fixed H_2O_2 and HRP concentration of 50 mM and 3.00 µg mL^{-1} are shown in Figure 1a,b. These graphs represent the impedance modulus (Z_{mod}) at 3×10^5 Hz as a function of time, t. Upon the addition of H_2O_2 at $t = 36$ s, the impedance sharply rises from 147.6 ± 0.9 Ω and then transitions into a plateau at 315.6 ± 10.2 Ω towards the end of the measurement (t ≈300 s).

Correspondingly, the Y_{mod} starts at about 6700 µS, followed by an almost linear decrease between 60–120 s after adding H_2O_2, and finally, leveling in a plateau of around 3200 µS. As shown in Equations (11) and (12), the admittance directly correlates with the degree of conversion of the precursor molecules from solution form into a gel. Therefore, the decrease of admittance value over time is a precise measure to evaluate the reaction kinetics, allowing the detailed investigation of the effects of the reactants and enzyme concentration on the gelation reaction.

2.3. Impedimetric Sensing of Different Concentration Effects on Gelation

In enzymatic gelation, the reaction rate is primarily influenced by temperature, the composition of the reaction medium, as well as substrate and enzyme concentrations. As temperature and the reaction medium are often fixed, particularly for in vivo applications, our study explores how varying concentrations of HRP, H_2O_2, and CMC-TA impact the gelation rate. Accordingly, a full factorial experimental design was established to evaluate further the effect of enzyme, precursor, and oxidant concentration on the gelation rate of the individual hydrogel formed. The gelation rates were compared by calculating the slope of Y_{mod} between 60 to 120 s, where the Y_{mod} shows a linear decrement.

First, the effects of varying HRP (0.25–10 µg mL^{-1}) and H_2O_2 (10–100 mM) concentrations on the measured slope, corresponding to the gelation rate, were evaluated (Figure 1d). The CMC-TA concentration was kept constant at 2.00% w/v. The bar chart given in Figure 1d represents that the magnitude of the slope of Y_{mod} increases with increasing HRP concentration from 0.25 to 3.00 µg mL^{-1}. After that, increasing the HRP concentration up to 10 µg mL^{-1} does not result in any additional increase in slope as it reaches a plateau. Specifically, when the HRP concentration increases from 0.25 to 3.00 µg mL^{-1} at 25 mM H_2O_2, the magnitude of the slope increases from 3.2 to 19.1 µS s^{-1} and then remains constant. As shown in Figure 1e, the slope linearly increases with increasing HRP concentration, which can be correlated to the enzymatic reaction rate being directly proportional to the enzyme concentration (Equation (8)). As the gelation rate increases, the conductivity decreases more rapidly due to reduced ion mobility. Further increment in enzyme concentrations above 3.00 µg mL^{-1} resulted in a plateau in slope. This phenomenon can be attributed to the cross-linked gel, which restricts the mobility of the substrate, subsequently limiting the enzymatic reaction. As

a result, the hindrance of mass transfer leads to a reduction in the reaction rate. Our results perfectly align with earlier findings, which all agreed that the gelation rate increases with increasing HRP concentration until a plateau is reached above a particular HRP concentration.[13,17,19,35–37]

Secondly, the effect of oxidant concentration on the gelation rate was investigated (Figure 1d). The data showed neither a consistent nor clear relation between the H_2O_2 concentration and the gelation rate. H_2O_2 is a substrate for HRP, but it also leads to the inactivation of the enzyme by oxidation.[38] Fortunately, the H_2O_2 inactivation of HRP follows significantly slower kinetics than the gelation reaction, and as the reaction time in our experiments was limited to only 6 min, such a detrimental effect could be avoided.[39] All utilized H_2O_2 concentrations are presumably much larger than the apparent K_{M,H_2O_2} for the reaction, as no concentration dependency of the reaction rate was observed (Figure 1d). No K_M values for this specific reaction were previously described. Yet, the previous report indicated that altering the H_2O_2 concentration between ≈9.8 and 49 mM does not affect the gelation rate of CMC-TA-pullulan-hydrogels.[33]

Ultimately, the effect of different precursor concentrations (0.125–3.50% w/v) on the measured slope was explored (Figure 1f). The slope increases with increasing precursor concentration and transitions into a plateau at higher precursor concentrations (> 2.00% w/v). For instance, for 1.00 µg mL^{-1} HRP and H_2O_2, the slope was elevated from 3.13 to 9.56 µS s^{-1} when increasing the precursor concentration from 0.125 to 2.00% w/v. The slope value remained nearly constant, regardless of the rise in precursor concentration above 2% w/v. The increasing trend of the slope can be explained by fundamental enzyme kinetics characterized by the Michaelis–Menten equation (Equation (8)). The substrate concentration, in this case, the precursor concentration, increases the enzymatic reaction rate until all enzymes are saturated. Another effect leading to a plateau is the viscosity, which increases with increasing precursor concentration, thereby reducing the reaction rate via decreasing the mobility of the enzyme and the substrate. Several groups working with HRP cross-linked hydrogels using tyramine-conjugated gelatin,[13] PEG,[17] dextran,[37] and alginate[19] precursors found a decrease in gelation time with increasing precursor concentration, implying an increased reaction rate.

2.4. Kinetic Modeling and Extraction of Kinetic Parameters from Impedance Data

For quantitative data analysis, a numerical model for the conductivity and the enzymatic reaction rate was derived (please refer to the Experimental Section). For all samples, it was confirmed that G_S did not differ by more than 10% from Y_{mod}. This enabled us to calculate the reaction rates and kinetic constants, as the conductivity in the first approximation is proportional to the concentration of the reactive species. The following numerical values were found by fitting the experimental data to the proposed model. In this study, $K_{M,CMC-TA}$ is referred to as simply K_M (**Table 1**).

Figure 2 compares the experimentally determined and the fitted Y_{mod} data versus time obtained for the gelation of 0.25%, 0.50%, and 2.00% w/v CMC-TA with 0.25, 1.00, and 3.00 µg mL^{-1} HRP. The graphs for the remaining CMC-TA concentrations

ADVANCED
SCIENCE NEWS
www.advancedsciencenews.com

ADVANCED
FUNCTIONAL
MATERIALS
www.afm-journal.de

Table 1. Fitted model parameters for the enzyme kinetic and conductivity.

Parameter	Value	Unit
$k_{\Lambda,precursor}$	0.583	–
k_{cat}	95.5	s^{-1}
k_D	0.000494	–
K_M	82.1	$\mu mol\ L^{-1}$

(0.125, 1.0, 1.5, 2.5, 3.0, and 3.5% w/v) can be found in the Supporting Information (Figure S5).

For all CMC-TA concentrations, Y_{mod} first decreases steeply and then transitions into a plateau over time. The shape of the curves and the plateau values can be accurately predicted with the proposed model (CV% < 10%, R^2 > 0.90). The time needed to reach the plateau (defined as the time duration until the reaction rate is 1% of its initial value) and the plateau values increase with increasing precursor concentration and decreasing enzyme concentration. For example, with 3.00 µg mL^{-1} HRP, the plateau time is 82 s for 0.25% w/v CMC TA, 120 s for 0.50% w/v CMC TA, and longer than 210 s for 2.00% w/v CMC-TA. The corresponding admittance plateau values experimentally measured at 210 s are 700.8 ± 9.44, 1037.4 ± 51.8, and 3670 ± 172.8, for 0.25%, 0.05%, and 2.00% w/v CMC-TA respectively. Similarly, the model-predicted plateau times are found as 73 s, 94 s, and

greater than 210 s, with respective admittance plateau values of 740.7, 1170.2, and 4032.4 µS for 0.25%, 0.50%, and 2.00% w/v CMC-TA, respectively.

To the best of our knowledge, K_M and k_{cat} values for HRP-mediated hydrogelation have only been investigated for small molecules such as Amplex Red,[40] guaiacol,[41] TMB,[42] OPD,[42] and phenol,[43] due to substrate quantification limitations. To make a relevant comparison, we examined the apparent K_M and k_{cat} values reported for HRP-mediated gelation of free phenol, which serves as the cross-linkable group in the CMC-TA, revealing values of 1.37 mM and 66.41 s^{-1}, respectively.[43] In contrast, our study determined K_M and k_{cat} values of 82.1 µM and 95.5 s^{-1} for the CMC-TA precursor.

Notably, the calculated K_M value corresponds to the molar concentration of CMC-TA, which, when recalculated for phenol concentration, amounts to 4.15 mM. Consequently, although k_{cat} values are similar, our study found the K_M to be three times higher than the previously reported value, implying a reduced affinity of HRP for the phenol groups within CMC-TA compared to free phenol. This discrepancy may also be ascribed to steric effects, as the phenol groups are situated on the polymer backbone, potentially impeding the accessibility of enzymes.

Besides kinetic parameters, we also calculated the predicted sol-gel conversion percentages of CMC-TA precursors according to the proposed kinetic model for solution conductivity (Equation (12)) (Figure 2d).
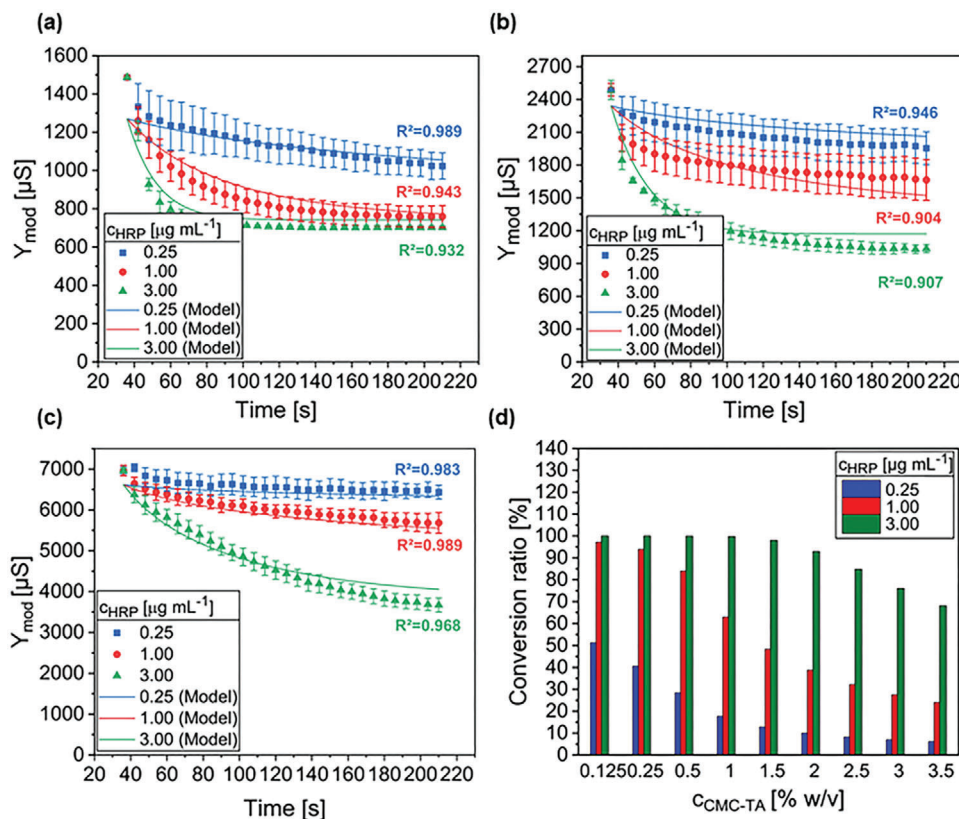
Figure 2. Experimentally determined and modeled time-course of the Y_{mod} for hydrogels consisting of a) 0.25, b) 0.50, and c) 2.00% w/v CMC-TA. The gelation reactions of various concentrations of CMC-TA were catalyzed by 0.25, 1.00, and 3.00 µg mL^{-1} HRP in the presence of 25 mM H$_2$O$_2$. d) The model predictions of sol-gel conversion percentages for CMC-TA concentrations range from 0.125% to 3.50% w/v at t = 210 s. The data points represent the mean values, and the error bars indicate the standard deviation of triplicated experiments (n = 3).

**ADVANCED
SCIENCE NEWS**

www.advancedsciencenews.com

**ADVANCED
FUNCTIONAL
MATERIALS**

www.afm-journal.de

In the presented data, two distinct trends emerge. Firstly, there is a noticeable increase in conversion with rising HRP concentration. To illustrate, for 3.00% w/v CMC-TA, the conversion percentage at $t = 210$ s escalates progressively from 10.1% to 27.5% and eventually peaks at 76.1%, corresponding to ascending HRP concentrations of 0.25, 1.00, and 3.00 µg mL^{-1}, respectively. Conversely, as precursor concentration increases, conversion percentage decreases. For instance, at a fixed HRP concentration of 3.00 µg mL^{-1}, complete conversion is attained for CMC-TA concentrations up to 1.50% w/v. Beyond this point, at higher precursor concentrations of 2.00, 2.50, 3.00, and 3.50% w/v, conversion percentages were recorded at 92.9%, 84.5%, 76.1%, and 68.2%, respectively.

The reduction in plateau time with increasing enzyme concentration can be attributed to Michaelis-Menten kinetics, which establishes a direct relationship between the enzymatic reaction rate and enzyme concentration. In contrast, the plateau time increases with elevating precursor concentration as the reaction rate fails to increase proportionally. Moreover, the reaction rate decreases as the absolute product concentration increases, resulting in a slowdown of precursor cross-linking. These effects also explain the observed effects of enzyme and precursor concentration on the modeled conversion percentage. Additionally, the predicted presence of plateaus without complete precursor conversion can be explained by the entrapment of the enzyme within the gel network, restricting its mobility and accessibility. When a specific cross-linking density is reached, the motion of the enzyme and uncross-linked precursor becomes so constrained that further reaction becomes impossible. This phenomenon is primarily observed at higher precursor concentrations ($\geq$ 2.00% w/v), where the cross-linking density and mesh size attain critical values. These findings show that the proposed model is not only fitted but is physicochemically meaningful and can predict complex reaction behavior.

2.5. Rheological Characterization
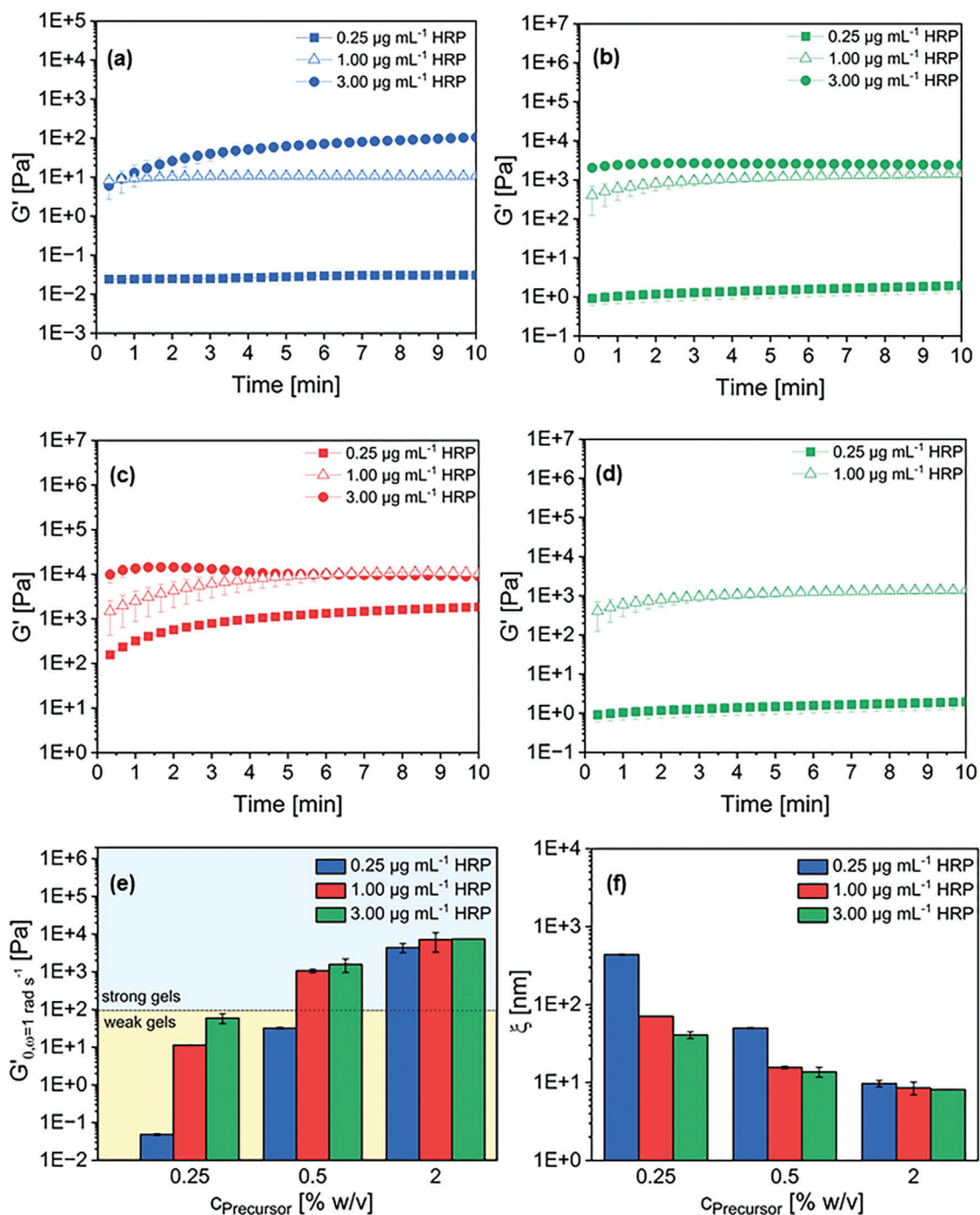
2.5.1. Bulk Characterization

Oscillatory shear measurements were conducted to investigate the effect of HRP and CMC-TA concentration on the gelation rate of enzymatically catalyzed hydrogels (**Figure 3**). The time sweeps given in Figure 3a–d show a clear distinction between weakly cross-linked hydrogels, which exhibit a weak gel-like response with a storage modulus (G') lower than 100 Pa, and strong gel-like hydrogels that manifest significant elasticity with a G' of above 100 Pa.

Regardless of HRP and CMC-TA concentrations, all samples reached the gel point, where the storage (G') and loss (G'') moduli become equal ($G' = G''$, data is displayed in Figures S6a–c, Supporting Information). The initial values of the elasticity modulus, $G'_{t=0}$, proportionally increased with increasing HRP and CMC-TA concentrations (Figure S6d, Supporting Information). Increasing the HRP concentration from 0.25 to 1.00 µg mL^{-1}, $G'_{t=0}$ notably escalated by factors of $\approx$330, 500, and 10 corresponding to 0.25, 0.50, and 2.00% w/v CMC-TA, respectively. When the HRP concentration is increased to 3.00 µg mL^{-1}, $G'_{t=0}$ shows similar values for 0.25% w/v CMC-TA (Figure 3a). How-

ever, $G'_{t=0}$ exhibits a relative increase by factors of around 7 and 5, at constant CMC-TA concentrations of 0.50 and 2.00% w/v, respectively (Figures 3b and 3c). These findings demonstrate that a far more cross-linked hydrogel network is already built within 1 min at HRP concentrations greater than 1.00 µg mL^{-1}, which together imply that the HRP concentration is a critical parameter for the gelation kinetics of the hydrogel. Hydrogels formed with higher concentrations than 1.00 µg mL^{-1} HRP and 0.50% w/v CMC-TA reached a plateau within 10 min. In contrast, hydrogels formed with 0.25 µg mL^{-1} HRP and 0.50% w/v CMC-TA, although hardly visible due to the logarithmic scale, still exhibit a slight increase in G' values after 10 min, as shown in Figure 3d. This can be elucidated through enzyme kinetics, which describes a linear correlation between the reaction rate and enzyme concentration, as we thoroughly discussed in the previous sections.

Higher $G'_{t=0}$ values are achieved for higher HRP concentration at a constant CMC-TA concentration, indicating an increased gelation rate. The same effect was found in conductivity measurements, where Y_{mod} decreased quickly for higher HRP concentrations (Figures 2 and 3f). Analog results are obtained when analyzing the effect of the increased CMC-TA concentration on hydrogelation. At 0.25 µg mL^{-1} HRP, when the CMC-TA concentration is increased from 0.25 to 2.00% w/v, $G'_{t=0}$ increases by a factor of 35 and 170, respectively. Likewise, at 1.00 µg mL^{-1} HRP, the increase is by a factor of 50 and 4, and at 3.00 µg mL^{-1} HRP, by a factor of 337 and 4, respectively. Once more, this agrees with our impedimetric analyses, where Y_{mod} decreased faster with increasing CMC-TA concentration (Figure 1f). This can be attributed to enzyme kinetics, where higher amounts of phenol groups serving as substrates lead to more rapid cross-linking. Here, it must be considered that similar results would have been observed by simply increasing the CMC concentration solely through concentration-driven physical cross-linking. However, the extent of the increase in $G'_{t=0}$ would have been much lower than the increase achieved through enzymatic cross-linking. Starting from a CMC-TA concentration of 2.00% w/v, a plateau in Y_{mod} slope was observed (Figure 1f). Therefore, the CMC-TA samples having a concentration higher than 2.00% w/v were not rheologically characterized.

In coherence with the previous time sweep data, frequency sweep data display an increase in the plateau modulus $G_{0,\omega=1rads^{-1}}$ as the concentrations of both HRP and CMC-TA increase (Figure 3e). The rise in the $G_{0,\omega=1rads^{-1}}$ is more pronounced when increasing the HRP concentration from 0.25 to 1.00 µg mL^{-1} in comparison to the increase observed from 1.00 to 3.00 µg mL^{-1}. Presumably, this is caused by the potential enzyme deactivation in the presence of H_2O_2. At high HRP concentrations, more CMC-TA precursor molecules could be cross-linked, allowing for a higher conversion before complete H_2O_2 deactivation. Moreover, a plausible explanation for the modest rise in $G_{0,\omega=1rads^{-1}}$ observed from 1.00 to 3.00 µg mL^{-1} HRP would be that the diffusion of the enzyme is hindered, due to the higher cross-linking density resulting in smaller mesh sizes of the hydrogels. This suggests that, at 1.00 µg mL^{-1} HRP concentration, the mesh size limit at which enzyme entrapment occurs was already attained. Thus, further precursor conversion from sol to gel form is prevented. This phenomenon is more prominent, particularly at high precursor concentrations, such as 2.00% w/v CMC-TA. The

**ADVANCED
SCIENCE NEWS**

www.advancedsciencenews.com

**ADVANCED
FUNCTIONAL
MATERIALS**

www.afm-journal.de

Figure 3. Time-dependent changes in the storage modulus (G') recorded by oscillatory shear measurements during the gelation reaction of varying CMC-TA samples are represented as a function of time, t, for 10 min. The effect of varying HRP concentrations ranging from 0.25 to 3.00 µg mL^{-1} on gelation kinetics of a) 0.25, b) 0.50, and c) 2.00% w/v CMC-TA precursor. d) The effect of different HRP concentrations (0.25 and 1.00 µg mL^{-1}) on the gelation kinetics of 0.50% w/v CMC-TA. The data is shown for 30 min. e) The plateau modulus, G_0, determined at $\omega = 1$ rad s^{-1}, and f) the estimated mesh size, ξ, is plotted as a function of CMC-TA concentration ($c_{precursor}$). The HRP concentration was varied from 0.25 to 3.00 µg mL^{-1} for each CMC-TA concentration. All gelation reactions were conducted with 25 mM H$_2$O$_2$. The data points represent the mean values, and the error bars indicate the standard deviation of replicated experiments ($n = 2$).

corresponding network mesh sizes of the formed hydrogels were estimated based on the classical theory of rubber elasticity,[44] as shown in Figure 3f. The mesh size of hydrogels formed with a 0.25% w/v CMC-TA and 0.25 µg mL^{-1} HRP was calculated as 437.59 ± 8.13 nm. Increasing the HRP concentration to 3.00 µg mL^{-1} reduces the mesh size to 40.80±4.12 nm. Additionally, increasing the CMC-TA concentration to 2.00% w/v decreases the mesh size to 8.15 ± 0.02 nm at 3.00 µg mL^{-1} HRP concentration. Therefore, high enzyme and precursor concentrations yield a higher cross-linking density. Consequently, this leads to a smaller mesh size comparable with the apparent hydrodynamic radius of HRP, which can be estimated at 6 nm based on proteins with a similar size.[45] More cross-links quickly formed stronger hydrogel networks at high HRP and CMC-TA concentrations. This reduced the enzyme mobility and led to a plateau in the gelation rate (Figure 1d). These findings support the assumption of the potential enzyme entrapment within the hydrogel network and explain the incomplete conversion of the CMC-TA precursor to hydrogel product at high concentrations (Figure 2d).

2.5.2. Multiple Particle Tracking (MPT)

Multiple particle tracking provides valuable insights into the viscoelastic and structural properties of hydrogels at a microscopic level and complements findings obtained with bulk rheology. In this study, the MPT experiments were performed on weak (**Figures** 4a,b) and highly elastic hydrogels (Figure 4c,d), which are categorized based on their bulk elasticity values being below (weak) or above (elastic) 100 Pa, respectively.

For all weak hydrogels (Figures 4a,b), the MSD traces vary almost linearly with time (slope ≈ 0.9), indicating that the motion of the tracer particles is purely diffusive and that the microenvironment surrounding the particles responds like a viscous liquid. This result can be explained by the smaller diameter of the tracer particles (≈200 nm) compared to the network mesh size (ξ) as estimated from bulk rheological measurements (Equation (13)). For the hydrogel comprising 0.25% w/v CMC-TA and 0.25 µg mL^{-1} HRP, ξ is estimated to be ≈432 nm, more than double the size of the tracer particles (Figure 4a–i). Under these conditions, the tracers cannot sense the network elasticity but the viscosity of the solution within the mesh. A similar explanation can be provided for hydrogels with compositions 0.25% w/v CMC-TA and 3.00 µg mL^{-1} HRP as well as 0.50% w/v CMC-TA and 0.25 µg mL^{-1} HRP (Figures 4a–ii,iii). In these two cases, ξ ≈50 nm is considered to be of the same order of magnitude relative to the tracer particle diameter, which did not allow for detecting the elasticity of the gel network. Indeed, in a typical MPT experiment, the diameter of the tracer particles must be at least 10 times larger than the network mesh size to accurately sense the elasticity of the gel network. Additionally, tracer particles can only explore low-viscosity regions for all weak elastic gels. Consequently, statistical analysis of the MSD distributions via van Hove diagrams revealed a homogeneous structure on the micrometer length scale with a non-Gaussian parameter, α<1. Overlay images obtained for corresponding hydrogels are shown in Figures 4b,d. In all images, but mainly for the hydrogel made of 0.25% w/v CMC-TA and 0.25 µg mL^{-1} HRP (Figure 4b–i),

black and white areas are visible, representing accessible and inaccessible regions for the tracer particles. These large white areas (≈5–20 µm) may correspond to densely cross-linked areas, where tracer particles are excluded due to the rapid cross-linking ($t < 1$ min), which indicates the heterogeneity of the gelation reaction.
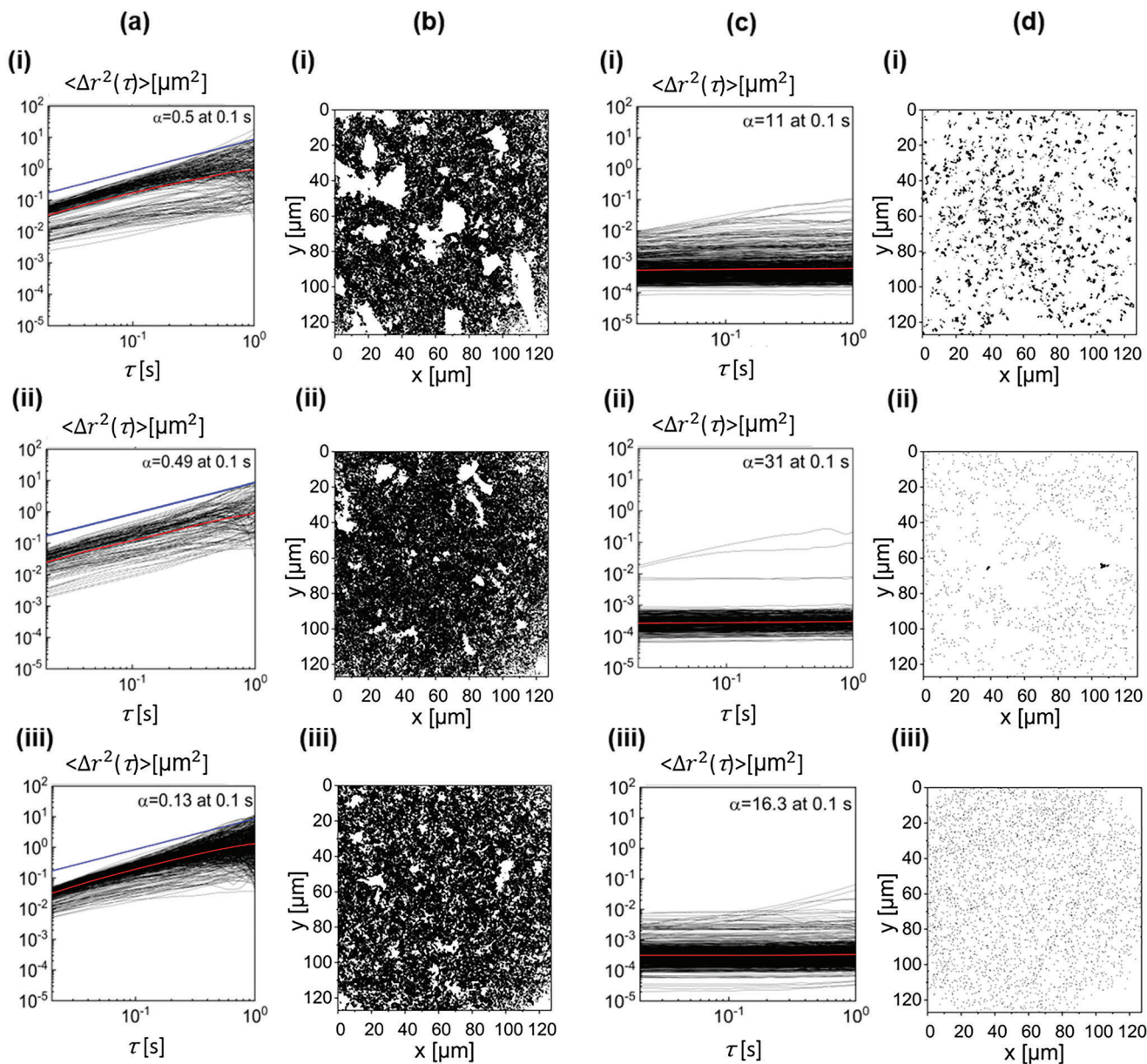
In summary, MPT and bulk rheology analyses suggest that the microstructure of the weak elastic gels mainly formed a loose polymeric network with a mesh size greater than 50 nm and a small fraction of the gel network exhibiting a higher degree of cross-linking.

A different behavior is observed for highly elastic hydrogels (Figures 4c,d). In detail, as the tracer particles having 200 nm diameter were much larger than the mesh size ($\xi < 20$ nm), all MSDs exhibit almost no time-dependence (slope ≈ 0), indicating that particles are well trapped in an elastic network (Figures 4c). In addition, we observe a relatively broad distribution of absolute MSD values greater than one (Figure 4c–ii) and two decades (Figures 4–i,iii), indicating a pronounced degree of heterogeneity of the network elasticity. This result is confirmed by high values of the non-Gaussian parameter, α, which is calculated as greater than 10 for all elastic gels. For instance, overlay images, particularly Figure 4d–ii, exhibit large white areas similar to the weak elastic gels (i.e., Figure 4b–i), corresponding to even more elastic regions inaccessible for the tracer particles. In summary, the microstructure of these highly elastic gels comprises a highly entangled polymeric network in several regions. In all cases, these regions are characterized by different cross-linking densities with a mesh size of less than 20 nm.

Finally, we evaluated the relation between plateau modulus (G') (indicating the elasticity of the formed gels) derived from rheological analysis, along with the hydrogel product concentration $c_{product}$ determined from EIS measurements and the developed kinetic model (Figure S7, Supporting Information). This relationship mostly reveals an initial linear increase in the modulus with product concentration, particularly indicative of enzymatic cross-linking, followed by a saturation point where further increases in product concentration do not significantly alter the G'. An empirical fit allows us to estimate the plateau modulus from the EIS data and the model with high reliability, evidenced by an R^2 value of 0.967.

For low CMC concentrations (≤ 0.50% w/v), the physical entanglement is the predominant source of the plateau of the formed gel. For higher CMC concentration (>0.50% w/v), the hydrogel formation is influenced by enzymatic cross-linking and physical entanglements of the polymer chains, as previously revealed by another study.[46] We hypothesize that the deviation from the empirical curve observed for 2.00% w/v CMC-TA and 0.25 µg mL^{-1} HRP arises from the physical entanglements becoming more pronounced than enzymatic crosslinking. Yet, even well-established rheological characterization methods cannot distinguish between these two different mechanisms that play a role in gel network formation. This observation highlights the semi-quantitative reliability of our validation approach, as it accurately reflects the expected behavior up to the point where physical entanglements begin to dominate the gel structure.

**ADVANCED
SCIENCE NEWS**

www.advancedsciencenews.com

**ADVANCED
FUNCTIONAL
MATERIALS**

www.afm-journal.de

Figure 4. a,c) MSD distributions and b,d) overlay images that are obtained from MPT analyses of CMC-TA hydrogels formed under varying precursor and enzyme concentrations. During gelation reactions, the H_2O_2 concentration was kept constant at 25 mM. The weak gels are composed of a–i,b–i) 0.25% w/v CMC-TA and 0.25 µg mL^{-1} HRP, a–ii,b–ii) 0.25% w/v CMC-TA and 3.00 µg mL^{-1} HRP, and a–iii,b–iii) 0.50% w/v CMC-TA and 0.25 µg mL^{-1} HRP. On the other hand, the strong elastic gels comprising c–i,d–i) 0.50% w/v CMC-TA and 3.0 µg mL^{-1} HRP, c–ii,d–ii) 2.00% w/v CMC-TA and 0.25 µg mL^{-1} HRP, and c–iii,d–iii) 2.00% w/v CMC-TA and 3.00 µg mL^{-1} HRP. The blue line represents the slope = 1, illustrating the purely viscous behavior of water. The red line refers to the median of the MSD distribution. α is the calculated non-Gaussian parameter for an individual MSD distribution.

3. Conclusion

In conclusion, this study positions EIS as a powerful tool for the real-time monitoring of enzymatic hydrogelation processes. By analyzing the gelation dependent impedimetric alterations of CMC-TA hydrogel precursors cross-linked by HRP and H_2O_2 at a fixed frequency of 3×10^5 Hz, we identified a method to detect hydrogelation reaction time course. This frequency was chosen for its reflection of the R_s, and significant changes in R_s upon gelation were measured, providing a direct quantitative insight into the reaction kinetics. Our findings, validated by rheological characterization, demonstrate that gelation rates increase with higher enzyme and precursor concentrations and, interestingly, are less influenced by the concentration of H_2O_2.

We have also developed a quantitative technique that combines the modified Michaelis–Menten kinetic model and conductance data, considering the reduced mobility of enzymes due to increased viscosity during the gelation reaction. This has allowed for the numerical calculation of precursor and product concentrations, accurately predicting conductivity changes. Notably,

**ADVANCED
SCIENCE NEWS**

www.advancedsciencenews.com

**ADVANCED
FUNCTIONAL
MATERIALS**

www.afm-journal.de

apparent K_M and k_{cat} values of 82.1 μM and 95.5 s^{-1}, respectively, were determined for CMC-TA cross-linked by HRP.

Overall, the EIS-based sensing methodology proposed herein transcends the capabilities of conventional rheological methods. It allows for real-time monitoring of hydrogelation reaction, providing a simplified yet refined approach. The technique requires minimal sample preparation, low sample volume demands, and is cost-efficient, making it an excellent choice for labs with limited resources. Additionally, it offers rapid and real-time data collection, enabling researchers to obtain results much faster than with standard optical methods. Moreover, this technique enables the precise determination of enzyme kinetics for enzymatically initiated hydrogelation reactions and holds the promise of becoming an indispensable tool for researchers in fields such as biomedicine and materials science.

Looking ahead, integrating EIS with microfluidics can pave the way for miniaturized high-throughput hydrogel screening platforms. Such an advancement would accelerate the discovery and optimization of smart hydrogels that can be dynamically tailored for specific applications.

4. Experimental Section

Materials: All chemicals and reagents were used as received without further purification. Carboxymethyl cellulose (CMC) sodium salt (MW = 90 kDa, DS = 0.7) was obtained from Thermo Fisher Scientific (Germany). Horseradish peroxide (HRP) type VI, N-(3-dimethylaminopropyl)-N′-ethyl carbodiimide-hydrochloride (EDC-HCl), N-hydroxysuccinimide (NHS), tyramine-hydrochloride (Tyr-HCl), sodium hydroxide (NaOH, 1.0 N), and hydrochloric acid (HCl, 36.5-38%) were purchased from Sigma Aldrich (Germany). 2-Morpholinoethanesulfonic acid monohydrate (MES) and ethanol were obtained from Merck (Germany). Hydrogen peroxide (H$_2$O$_2$) 3.4% w/w was purchased from VWR Chemicals (Germany). The fluorescent tracer particles used for multiple particle tracking (polystyrene microspheres, Dragon Green, 0.19 μm) were obtained from Bangs Laboratories (USA). Dialysis tubes with a 3.5 kDa molecular weight cut-off (MWCO) were purchased from Merck (Germany).

Synthesis and Characterization of Carboxymethyl Cellulose-Tyramine Conjugates (CMC-TA): Carboxymethyl cellulose-tyramine conjugates (CMC-TA) were synthesized by slightly modifying the previously described method.[35] Briefly, 50 mM MES buffer was prepared, and the pH was adjusted to 6.0 using 1 M NaOH and 1 M HCl. An appropriate amount of CMC was dissolved in the MES buffer to procure 1% w/v (45.8 mM carboxyl groups) solution by magnetically stirring at 1000 rpm for at least 3 h. Then, 45.8 mM Tyr-HCl was added, and the mixture was stirred for another 20 min at 300 rpm. Subsequently, 22.9 mM NHS and 45.8 mM EDC-HCl were added to initiate the synthesis. The resultant mixture was stirred for 24 h at 300 rpm at 25 °C. Moreover, the prepared mixture was dialyzed against ultrapure water (UPW) for three days to remove unreacted educts.

To assess the efficacy of the synthesis and purification procedures, the unconjugated CMC and purified CMC-TA samples were examined via UV–vis spectroscopy analyses. First, unconjugated CMC was used for the baseline recording. Then, the amount of incorporated tyramine (TA) within the CMC-TA conjugate was estimated by screening the TA-specific absorbance peak at 275 nm wavelength. Also, the dialysis buffer was analyzed to confirm the complete removal of unbound tyramine.

Proton nuclear magnetic resonance (^{1}H-NMR) spectroscopy analyses were conducted to confirm the tyramine incorporation into the CMC polymer backbone. Tyramine-HCl (20 mM), unconjugated CMC (0.50% w/v), and tyramine-conjugated CMC (CMC-TA, 0.50% w/v) were analyzed. Before analysis, all samples were dissolved in deuterium oxide (D$_2$O) containing 10 mM 3-(Trimethylsilyl)propanoic acid (TMSP) internal reference

compound. Subsequently, 1 mL of each sample was transferred into 5 mm NMR tubes. NMR spectral recordings were carried out under a magnetic field strength of 11.7 T, corresponding to a ^{1}H resonance frequency of 500 MHz.

Hydrogelation Screening by Impedimetric Analysis and Assay Development: Non-Faradaic EIS was selected to investigate the applicability of the impedimetric detection approach for hydrogelation monitoring. Interdigitated electrodes (IDEs) (IDE1-Au, MicruX, Spain) comprising 90 pairs of interdigitated electrode fingers with a width and gap size of 10 μm were used for impedimetric signal transduction. After cleaning with isopropanol and UPW, the IDEs were purged with nitrogen gas for drying. Before performing experiments, each IDE was inserted into a 3D-printed holder and linked to the potentiostat (Reference 600, Gamry Instruments, USA). The Bode spectrum of each tested sample was recorded by Gamry Framework Data Acquisition Software (v.7.2). All potentiostatic EIS and single frequency analyses were conducted at 25 mV of AC voltage by scanning the frequency range from 1×10^6 to 1 Hz.

The enzymatic cross-linking of the CMC-TA precursor was carried out on the IDE surface in the presence of HRP (3.00 μg mL^{-1}) and H$_2$O$_2$ (25 mM). Potentiostatic EIS analyses were performed to investigate the variations in electrical properties of the CMC-TA before and after gelation. Briefly, 27.2 μL of 2.00% w/v CMC-TA precursor solution was mixed with 3.4 μL of an HRP solution in a vial by gentle pipetting. Subsequently, 22.5 μL of this mixture was transferred onto the IDE surface, and the initial potentiostatic scan was executed. Following, 2.5 μL of H$_2$O$_2$ was introduced to initiate gelation, and the second potentiostatic scan was conducted. The Bode spectra obtained before and after the CMC-TA precursor gelation were analyzed by fitting to the model equivalent circuit model using Gamry Echem Analyst Software (v.7.8.2, Gamry Instruments, USA). Numerical values for model circuit elements: double-layer capacitance (CPE_{DL}), geometric capacitance (C_{geo}), and the solution resistance (R_s) were extracted.

Secondly, an innovative approach for real-time hydrogelation monitoring based on single-frequency analysis was established. 3×10^5 Hz was selected as the frequency to perform single-frequency analyses since, at this point, the impedance values of the tested samples before and after gelation consisted only of the resistive component. For testing, 22.5 μL of CMC-TA and HRP mixture was dropped onto the IDE, and the first potentiostatic EIS scan was performed. Then, adjacent single-frequency analyses were carried out at 3×10^5 Hz constant frequency by applying an AC voltage of 25 mV. To initiate the hydrogelation reaction, 2.5 μL of H$_2$O$_2$ solution was added to the CMC-TA and HRP mixture. Following the single frequency measurement, another potentiostatic scan was performed to screen the impedance spectra of each sample post-gelation.

Moreover, a full factorial experimental design was conducted to explore the effect of varying CMC-TA, HRP, and H$_2$O$_2$ concentrations on the gelation rate. Initially, the impact of HRP and H$_2$O$_2$ concentration on the gelation rate of CMC-TA was investigated. CMC-TA concentration was kept constant at 2.00% w/v, while HRP and H$_2$O$_2$ concentrations were systematically varied between 0.25 and 10.0 μg mL^{-1} and 10 and 100 mM, respectively. Subsequently, the effect of precursor concentration on the gelation rate was examined across varying CMC-TA and HRP concentrations spanning the ranges of 0.125–3.50% w/v and 0.25–3.00 μg mL^{-1}. At this step, the H$_2$O$_2$ concentration was kept constant at 25 mM. The three-step screening protocol was applied to all sample groups. The measurements were conducted at room temperature (19 ± 2 °C). The three-step experimental protocol established for hydrogelation monitoring is sketched in Figure S4, Supporting Information.

Kinetic Modeling of the Hydrogelation and Extraction of Kinetic Parameters from the Impedance Data: Model equations were derived to facilitate the quantitative analysis of the gelation reaction and for extracting kinetic parameters. The dataset encompasses impedimetric readings acquired during the impedimetric testing of varied concentrations of the CMC-TA precursor, ranging from 0.125% to 3.50% w/v, and HRP concentrations of 0.25, 1.00, and 3.00 μg mL^{-1}. The H$_2$O$_2$ concentration remained constant at 50 mM.

**ADVANCED
SCIENCE NEWS**

www.advancedsciencenews.com

**ADVANCED
FUNCTIONAL
MATERIALS**

www.afm-journal.de

First, the recorded impedance modulus Z_{mod} was converted into the admittance modulus (Y_{mod}) using Equation (1).

$$Y_{mod} = \frac{1}{Z_{mod}} \tag{1}$$

The Y_{mod} at the selected frequency of 3×10^5 Hz primarily comprised the real part of the admittance, corresponding to the electrolyte conductivity, G_S. It was observed that the calculated G_S values for the tested samples did not significantly differ from Y_{mod} ($\approx 10\%$). Therefore, for further analysis, the following simplification was done (Equation (2)).

$$Y_{mod} \sim G_S \tag{2}$$

where G_S is the sum of the conductivity G_i of each component in the solution to which the IDEs were exposed (Equation (3)).

$$G_S = G_{precursor} + G_{product} + G_{enzyme} + G_{UPW} + G_{H2O2} + G_{salt} \tag{3}$$

The significant contributions to electrolyte conductivity primarily arose from the precursor and the reaction product (hydrogel). On the other hand, given the precursor's dialysis, the solution comprised no free salts, and the manufacturer specified the enzyme HRP as salt-free. Therefore, Equation (3) was simplified to Equation (4).

$$G_S = G_{precursor} + G_{product} = \Lambda_{precursor}c_{precursor} + \Lambda_{product}c_{product} \tag{4}$$

The conductivity of a substance i was determined by its molar conductivity (Λ_i) multiplied by its concentration (c_i). Here, it might be considered that molar conductivity itself depends on the concentration of the substance. The correlation was determined by calculating the molar conductivities of various CMC-TA concentrations (0.125–3.50% w/v) using the conductivity data obtained by potentiostatic EIS analyses and fitting the respective dependency on precursor concentrations using a power function (Equation (5)). The empirical fit was selected because of the high molecular weight and multiple valencies of the precursor molecules, which could only be described with complex theoretical models. The following values for the parameters of the power function describing the molar conductivity of CMC-TA were extracted from the fitted curve: $a = 104.8$ µS·µM^b, $b = 0.229$. The associated graphs are given in the Supporting Information (Figure S8).

$$\Lambda_{precursor} = ac_{precursor}^{-b} \tag{5}$$

In the first approximation, the total number of charges did not change during the gelation reaction of precursor molecules forming a hydrogel as the product. This meant that if a dimer was created by cross-linking two precursor molecules, it would carry double charges. Yet, the number of charges per precursor unit fixed within the product remained constant. Therefore, by defining an effective product concentration in a way that it corresponds with the concentration of precursor units fixed within the product, the consideration of the contribution of the product in the total conductivity, G_S, could be described simply by Equation (4), no matter if dimers, trimers or larger oligomers were formed. In addition, the effective concentration of precursor units fixed in the product could be easily derived from the concentration decline of the precursor molecules (Equation (6)).

$$c_{eff,product} = c_{precursor} (ta = 0) - c_{precursor} (t) \tag{6}$$

The molar conductivity of the precursor units fixed within the product ($\Lambda_{eff,product}$) was assumed to be a constant fraction of the precursor molar conductivity (Equation (7)).

$$\Lambda_{product} = k_{\Lambda,product}\Lambda_{precursor} \tag{7}$$

The conductivity reduction was hypothesized to arise from the increased size of the cross-linked product molecules. $k_{\Lambda,product}$ represented an average value of the molar conductivity reduction factors of different product molecules with varying chain lengths and number of cross-linkages. Although it was a straightforward simplification, in the analysis, Λ values were assumed to be constant during an experiment.

A modified Michaelis–Menten equation was used to model the enzymatic reaction rate (Equation (8)).

$$\frac{dc_{precursor}}{dt} = c_{HRP}k_{cat,eff} \frac{c_{precursor}}{K_M + c_{precursor}} \tag{8}$$

where $c_{precursor}$ is the precursor concentration in µM, c_{HRP} is the HRP concentration in µM, $k_{cat,eff}$ is the effective catalytic constant of the enzyme in s^{-1}, and K_M is the Michaelis–Menten constant for CMC-TA in µM. Only the precursor was considered a substrate for reaction kinetics because H$_2$O$_2$ was surplus in the reaction medium.

The enzymatic reaction shaped the polymeric network and the corresponding viscosity increased. Both effects impeded the accessibility of the enzyme, thereby limiting its apparent activity. The reduction of the apparent activity could be expressed by the reduction of the effective rate constant, with the degree of reduction depending on the ratio between the formed product and the applied amount of enzyme. The experiments showed that this dependency was not linear, meaning that small amounts of cross-linked precursor showed almost no effect. However, the rate constant quickly decayed beyond a specific $c_{product}$ to c_{HRP} ratio. In the analysis, this non-linear behavior was accounted for by applying an exponential correlation with the deactivation constant, k_D, as shown in Equation (9).

$$k_{cat,eff} = k_{cat}e^{-k_D c_{product}/c_{HRP}} \tag{9}$$

According to the equations given above, the established model describing the conductivity decay during enzymatically catalyzed hydrogelation involved four parameters: $k_{\Lambda,precursor}$, k_{cat}, k_D, and K_M. To determine these parameters, numerical calculations were performed for the time course of precursor and product concentrations, as well as the corresponding admittance. For all N time points, with an interval length $\Delta t = 1$ s, $c_{product,n}$ at the nth time point were calculated using the reaction rate ($\frac{dc_{precursor}}{dt}$) and the precursor concentration at the previous time point ($c_{precursor,n-1}$) using Equation (10).

$$c_{precursor,n} = c_{precursor,n-1}$$
$$- c_{HRP}k_{cat}e^{-k_D c_{product,n-1}/c_{HRP}} \frac{c_{precursor,n-1}}{K_M + c_{precursor,n-1}}\Delta t \tag{10}$$

The predicted $\hat{Y}_{mod,n} = \hat{G}_{s,n}$ was calculated for each time step using Equation (4). The model parameters ($k_{\Lambda,precursor}$, k_{cat}, k_D, and K_M) were fitted to the experimental data with Microsoft Excel Solver using the generalized reduced gradient (GRG) algorithm. The objective was to minimize the sum of squared errors between the fit and experimental data for all data points in the complete dataset.

To assess the goodness of the fit, the coefficient of determination (R^2) for each parameter combination was calculated using Equation (11).

$$R^2 = 1 - \frac{\sum_{n=1}^{N} \left(Y_{mod,n} - \hat{Y}_{mod,n}\right)^2}{\sum_{n=1}^{N} \left(Y_{mod,n} - \bar{Y}_{mod}\right)^2} \tag{11}$$

where $Y_{mod,n}$ is the experimentally determined admittance at the nth time point, $\hat{Y}_{mod,n}$ is the predicted admittance of the model at the nth time point, and $\bar{Y}_{mod}$ is the average of the experimentally determined admittance values for all time steps (N). Lastly, the sol-gel conversion percentage, %$X_{precursor}$, was calculated using Equation (12). $c_{precursor}$ at $t = 210$ s, the endpoint of single frequency analysis was considered for calculation.

$$\%X_{precursor} = \frac{c_{precursor,t=0} - c_{precursor,t=210s}}{c_{precursor,t=0}} \times 100 \tag{12}$$

ADVANCED
SCIENCE NEWS

www.advancedsciencenews.com

ADVANCED
FUNCTIONAL
MATERIALS

www.afm-journal.de

Bulk Rheology: A rotational rheometer (Physica MCR 501, Anton Paar) equipped with cone-plate (diameter 50 mm, cone angle 4°) and plate-plate (diameter 8 mm) measuring cells was used to perform small amplitude oscillatory shear experiments on hydrogels with different degrees of elasticity, namely from weak to strong gels, respectively. For all hydrogels, frequency sweeps, covering the frequency range from 0.2 to 100 rad s^{-1}, were performed at strain amplitude sufficiently small enough to provide a linear material response. From these modulus curves, the elastic plateau modulus, G_0, was determined as the storage modulus, G', at 1 rad s^{-1} frequency, exhibited a constant plateau. By subtracting the G_0 values obtained for each tested sample into Equation (13), the individual mesh size (ξ) of the hydrogel networks was calculated.[44]

$$\xi = \left(\frac{k_B T}{G_0} \right)^{1/3} \tag{13}$$

where k_B is the Boltzmann constant in J K^{-1} and T is the absolute temperature in K. In addition, time sweep tests were performed to characterize the hydrogelation kinetics. Each CMC-TA-HRP mixture was placed directly on the lower plate of the measuring system. The H$_2$O$_2$ was added to this mixture to initiate gelation. The upper cone or plate was then contacted with the tested sample. The variation in viscoelastic moduli as a function of time concerning the linear viscoelastic regime was analyzed at a constant shear frequency and strain amplitude. All measurements were conducted at 20 °C, and temperature was controlled by a thermostat (Eco Silver, Lauda).

Microrheology–Multiple Particle Tracking (MPT): Besides macrorheological properties, MPT-based microrheology was a well-established method for characterizing microstructural and local viscoelastic properties of materials. The principle relied on measuring the Brownian motion of probe particles embedded in the sample to extract its rheological properties.

The MPT setup used in this study was based on an inverted fluorescence widefield microscope (Axio Observer D1, Carl Zeiss, Germany) equipped with a Fluar objective (numerical aperture 1.3, 100× magnification, oil immersion lens, Carl Zeiss, Germany).[47] Green fluorescent polystyrene microspheres of 0.2 μm diameter with a 1.06 g cm^{-3} density were used as tracer particles (Bangs Laboratories, USA). The sample containing the investigated hydrogel, including the tracers, was injected into a self-built chamber consisting of a coverslip and microscope glass slide. 2D images (field of view 127 × 127 μm, frame rate of 50 frames per s^{-1}) of the fluorescent particles were recorded using a sCMOS camera Zyla X (Andor Technology, UK). Movies of the fluctuating microspheres were analyzed using a custom MPT routine incorporated into the software Image Processing System (Visiometrics iPS), which located the center of mass [$x(t)$, $y(t)$] of each particle in every picture and allowed the construction of particle trajectories.[48,49] According to conventional analysis, that is, discarding all short particle trajectories, individual time-averaged mean square displacement (MSD) values were calculated using a self-written Matlab® program based on the widely used Crocker and Grier tracking algorithm with $\langle \Delta r^2 (\tau) \rangle = \langle [x(t+\tau) - x(t)^2] + [y(t+\tau) - y(t)^2] \rangle$ where τ is the time lag and t is the elapsed time.[47,50,51] To characterize the heterogeneity of the hydrogel microstructure, a statistical analysis of the MSD distribution was performed by extracting the non-Gaussian parameter $\alpha = \frac{\langle x^4 (\tau) \rangle}{3 \langle x^2 (\tau) \rangle^2} - 1$, in which x^4 and x^2 are the fourth and second moments of the probability distribution of particle displacement.[52] α was zero for a Gaussian distribution as expected for an ergodic homogeneous, uniform sample, while broader distributions resulted in large α values.

Supporting Information

Supporting Information is available from the Wiley Online Library or from the author.

Conflict of Interest

The authors declare no conflict of interest.

Data Availability Statement

The data that support the findings of this study are available from the corresponding author upon reasonable request.

[1] A. S. Hoffman, *Adv. Drug Delivery Rev.* **2012**, *64*, 18.
[2] S. Van Vlierberghe, P. Dubruel, E. Schacht, *Biomacromolecules.* **2011**, *12*, 1387.
[3] F. Yang, J. Zhao, W. J. Koshut, J. Watt, J. C. Riboh, K. Gall, B. J. Wiley, *Adv. Funct. Mater.* **2020**, *30*, 2003451.
[4] Y. Liang, J. He, B. Guo, *ACS Nano* **2021**, *15*, 12687.
[5] L.-B. Jiang, D.-H. Su, S.-L. Ding, Q.-C. Zhang, Z.-F. Li, F.-C. Chen, W. Ding, S.-T. Zhang, J. Dong, *Adv. Funct. Mater.* **2019**, *29*, 1901314.
[6] L. Shi, F. Wang, W. Zhu, Z. Xu, S. Fuchs, J. Hilborn, L. Zhu, Q. Ma, Y. Wang, X. Weng, D. A. Ossipov, *Adv. Funct. Mater.* **2017**, *27*, 1700591.
[7] E. Mancha Sánchez, J. C. Gómez-Blanco, E. López Nieto, J. G. Casado, A. Macías-García, M. A. Díaz Díez, J. P. Carrasco-Amador, D. Torrejón Martín, F. M. Sánchez-Margallo, J. B. Pagador, *Front. Bioeng. Biotechnol.* **2020**, *8*, 776.
[8] T. R. Hoare, D. S. Kohane, *Polymer* **1993**, *49*, 2008
[9] A. Herrmann, R. Haag, U. Schedler, *Adv. Healthcare Mater.* **2021**, *10*, 2100062.
[10] L. Sun, Y. Zhong, J. Gui, X. Wang, X. Zhuang, J. Weng, *Int. J. Nanomed.* **2018**, *13*, 843.
[11] L. S. M. Teixeira, J. Feijen, C. A. van Blitterswijk, P. J. Dijkstra, M. Karperien, *Biomaterials* **2012**, *33*, 1281.
[12] S. Sakai, Y. Ogushi, K. Kawakami, *Acta Biomater.* **2009**, *5*, 554.
[13] S. Sakai, K. Hirose, K. Taguchi, Y. Ogushi, K. Kawakami, *Biomaterials* **2009**, *30*, 3371.
[14] S. Xu, Q. Li, H. Pan, Q. Dai, Q. Feng, C. Yu, X. Zhang, Z. Liang, H. Dong, X. Cao, *ACS Biomater. Sci. Eng.* **2020**, *6*, 6896.
[15] K. S. Kim, S. J. Park, J.-A. Yang, J.-H. Jeon, S. H. Bhang, B.-S. Kim, S. K. Hahn, *Acta Biomater.* **2011**, *7*, 666.
[16] K. Xu, F. Lee, S. J. Gao, J. E. Chung, H. Yano, M. Kurisawa, *J. Controlled Release* **2013**, *166*, 203.
[17] K. Moriyama, R. Wakabayashi, M. Goto, N. Kamiya, *Biochem. Eng. J.* **2015**, *93*, 25.
[18] A. Schulz, M. M. Gepp, F. Stracke, H. von Briesen, J. C. Neubauer, H. Zimmermann, *J. Biomed. Mater. Res., Part A* **2019**, *107*, 114.

**ADVANCED
SCIENCE NEWS**

www.advancedsciencenews.com

**ADVANCED
FUNCTIONAL
MATERIALS**

www.afm-journal.de

[19] J. Hou, C. Li, Y. Guan, Y. Zhang, X. X. Zhu, *Polym. Chem.* **2015**, *6*, 2204.

[20] E. Lih, J. S. Lee, K. M. Park, K. D. Park, *Acta Biomater.* **2012**, *8*, 3261.

[21] J. W. Bae, J. H. Choi, Y. Lee, K. D. Park, *J. Tissue Eng. Regener. Med.* **2015**, *9*, 1225.

[22] Z. Luo, Y. Wang, J. Li, J. Wang, Y. Yu, Y. Zhao, *Adv. Funct. Mater.* **2023**, *33*, 2306554.

[23] N. C. Veitch, *Phytochemistry* **2004**, *65*, 249.

[24] V. Nele, J. P. Wojciechowski, J. P. K. Armstrong, M. M. Stevens, *Adv. Funct. Mater.* **2020**, *30*, 2002759.

[25] J. M. Zuidema, C. J. Rivet, R. J. Gilbert, F. A. Morrison, *J. Biomed. Mater. Res.* **2014**, *102*, 1063.

[26] J. A. McGlynn, N. Wu, K. M. Schultz, *J. Appl. Phys.* **2020**, *127*, 201101.

[27] B. R. Denzer, R. J. Kulchar, R. B. Huang, J. Patterson, *Gels* **2021**, *7*, 158.

[28] S. Seibt, S. With, A. Bernet, H.-W. Schmidt, S. Förster, *Langmuir* **2018**, *34*, 5535.

[29] X.-F. Yan, M.-H. Wang, D. An, *Chin. J. Anal. Chem.* **2011**, *39*, 1601.

[30] L. A. Middlemiss, A. J. Rennie, R. Sayers, A. R. West, *Energy Rep.* **2020**, *6*, 232.

[31] V. Encinas-Sánchez, M. T. de Miguel, M. I. Lasanta, G. García-Martín, F. J. Pérez, *Sol. Energy Mater. Sol. Cells* **2019**, *191*, 157.

[32] S. S. Hegde, B. Jeevan Fernandes, V. Talapatadur, K. P. Ramesh, K. Ramesh, *Mater. Today: Proc.* **2022**, *62*, 5648

[33] S. Bang, Y.-G. Ko, W. I. Kim, D. Cho, W. H. Park, O. H. Kwon, *Int. J. Biol. Macromol.* **2017**, *105*, 886.

[34] I. S. D. Santos-Neto, C. D. Carvalho, G. B. A. Filho, C. D. S. S. Andrade, G. C. d. O. Santos, A. K. Barros, J. V. d. F. Neto, V. L. P. Casas, L. M. R. Alencar, A. J. O. Lopes, F. C. Silva, F. S. M. Sinfrônio, *Sensors* **2021**, *21*, 7288.

[35] Y. Ogushi, S. Sakai, K. Kawakami, *J. Biosci. Bioeng.* **2007**, *104*, 30.

[36] M. Kurisawa, J. E. Chung, Y. Y. Yang, S. J. Gao, H. Uyama, *Chem. Commun.* **2005**, *34*, 4312.

[37] R. Jin, C. Hiemstra, Z. Zhong, J. Feijen, *Biomaterials* **2007**, *28*, 2791.

[38] K. J. Baynton, J. K. Bewtra, N. Biswas, K. E. Taylor, *Bioch. Biophys. Acta* **1994**, *1206*, 272.

[39] D. Morales-Urrea, A. López-Córdoba, E. M. Contreras, *Sci. Rep.* **2023**, *13*, 13363.

[40] M. Glettenberg, C. M. Niemeyer, *Bioconjugate Chem.* **2009**, *20*, 969.

[41] J. Ostojić, S. Herenda, Z. Bešić, M. Miloš, B. Galić, *Molecules* **2017**, *22*, 1120.

[42] W. M. Aumiller, B. W. Davis, E. Hatzakis, C. D. Keating, *J. Phys. Chem.* **2014**, *118*, 10624.

[43] P. T. Vasudevan, L. O. Li, *Appl. Biochem. Biotechnol.* **1996**, *60*, 203.

[44] M. Rubinstein, *Polymer Physics*, Oxford University Press, Oxford **2014**.

[45] H. P. Erickson, *Biol. Proced. Online* **2009**, *11*, 32.

[46] C. G. Lopez, W. Richtering, *Carbohydrate* **2021**, *267*, 118117.

[47] A. Kowalczyk, C. Oelschlaeger, N. Willenbacher, *Polymer* **2015**, *58*, 170.

[48] R. Bubeck, C. Bechinger, S. Neser, P. Leiderer, *Phys. Rev. Lett.* **1999**, *82*, 3364.

[49] S. Neser, C. Bechinger, P. Leiderer, T. Palberg, *Phys. Rev. Lett.* **1997**, *79*, 2348.

[50] C. Oelschlaeger, J. Marten, F. Péridont, N. Willenbacher, *J. Rheol.* **2022**, *66*, 749.

[51] J. C. Crocker, D. G. Grier, *J. Colloid Interface Sci.* **1996**, *179*, 298.

[52] E. R. Weeks, J. C. Crocker, A. C. Levitt, A. Schofield, D. Weitz, *Science* **2000**, *287*, 627.